Methods for Hemodynamic Parameters Measurement using the Laser Speckle Effect in Macrocirculation

Pedro G. Vaz[1,2], Anne Humeau-Heurtier[2], Edite Figueiras[3] and João Cardoso[1]

[1]LIBPhys-UC, Department of Physics, University of Coimbra
Rua Larda, Coimbra 3004-516, Portugal
[2]University of Angers, LARIS - Laboratoire Angevin de Recherche en Ingénierie des Systèmes,
62 avenue Notre-Dame du Lac, 49000 Angers, France
[3]International Iberian Nanotechnology Laboratory, Avenida Mestre José Veiga, s/n,
4715-330, Braga, Portugal
pvaz@uc.pt, jmrcardoso@uc.pt, anne.humeau@univ-angers.fr,
edite.figueiras@inl.int

Abstract. This chapter present a set of studies that have been developed with the goal of probing the possibilities of using laser speckle effect as a tool to extract macrocirculatory hemodynamic parameters. Within this project, a laser speckle prototype has been constructed and three bench experiment have been designed. The first bench experiment consists on using multi-wavelength light sources to extract the vibration frequency of a phantom and heart rate of several subjects. The second experiment consists on the extraction of the pulse pressure waveform using the same instrumentation and processing algorithms as the ones used on microcirculation laser speckle imaging. Finally, a pilot study was also designed in order to use laser speckle for 2D image segmentation. The obtained results revealed that laser speckle has the capability to extract macrocirculatory hemodynamic parameters and that this feature can be included in commercially available devices. In this sense, the ability to extract macrocirculatory and microcirculatory parameters could lead to interesting commercial advantages.

1 Introduction

Laser speckle has been considered as a side effect of using polarized light since the first laser based applications. Speckle can be defined as the visualization of a dark and bright dot pattern resulting from the interference of the coherent light when it is reflected by a rough surface or liquid media containing scatterers. This effect limits the contrast, spatial resolution and signal-to-noise ratio (SNR) of laser based applications such as optical coherence tomography (OCT) [1]. However, for a long time that speckle imaging has been used as source of important information. It has been used as static material characterization technique because it contains information on the surface morphological properties [2] and also on dynamic material strain characterization [3].

The first reference of a biomedical application of laser speckle imaging (LSI) can be found in the pioneer work of Fercher and Briers (1981) [4] where speckle was used to analyze the retina blood flow, a typical application for microcirculation assessment. Since then, LSI has been studied and improved by many researchers that believe this

technique is able to provide important physiological informations with benefits over the existing methods. Most works related with LSI still focus on the assessment of blood flow inside small arteries, either in the development of new LSI instrumentation or improving the existing mathematical theories. Most LSI scientific research relates with the two major technique issues, which are the improvement of its assessment depth and the determination of quantitative blood flow values.

The following paragraphs summarize some reference works on LSI during the past two decades in order to give an overview of current situation. David Boas and Andrew Dunn have developed many important works on LSI, one in particular, Boas and Dunn (2010) [5], presents an important explanation of the laser speckle imaging physics. Parthasarathy *et al.* [6] proposed an accurate LSI technique based on the acquisition of the speckle patterns using multiple exposure times. This same technique has also been explored by Kazmi *et al.* [7] several years later. Ramirez-San-Juan *et al.* [8] have studied the influence of static scatterers in two LSI image analysis methods, the spatial and temporal laser speckle contrast. The effect of static scatterers is an important research line also explored by Zahkarov *et al.* [9] by developing new theoretical concepts to correct this effect. Varma *et al.* [10] and Huang *et al.* [11] presented works on laser speckle tomography, which is a recently developed LSI variation that improves the assessment depth of speckle imaging. Some LSI methodological reviews have been presented by Senarathna *et al.* [12], Briers *et al.* [13] and Vaz *et al.* [14]. Finally, the latest developments on laser speckle research ranging from theoretical analysis to practical application can be found in [15–18].

Laser speckle imaging has been strongly focused on microcirculatory applications but it can also be used as a tool for macrocirculatory assessment. This chapter starts by introducing some simple laser speckle imaging theoretical (section 2) concepts necessary for the comprehension of the experiments. Next, an overview of physiological concepts (section 3) related with the macrocirculation physiology is presented. After that, the experimental tests, developed for proof of concept, will be presented (section 4) and their results discussed (section 5). Finally, the conclusions are presented in section 6.

2   Laser Speckle Imaging

2.1   Instrumentation Set-up

The LSI technique is often based on the illumination of a sample using a coherent light source, as a laser, and the detection of the reflected light using a video camera. In order to analyzed samples with large areas, a beam expander needs to be coupled onto the laser beam. To these two critical elements, adds up a signal processing and control module which can be a standard PC or dedicated hardware. This module is responsible for the image collection, from the video camera, and is responsible for digitally process them in order to extract valuable information. Figure 1 represent a standard LSI instrumentation.

Figure 2 shows an example of a synthesized laser speckle pattern of a static target with 800×600 pixels. This figure has been synthesized using the algorithm described in [19]. The dark and bright spots are clearly visible in this figure and, since it results from a static target, they are very sharp.
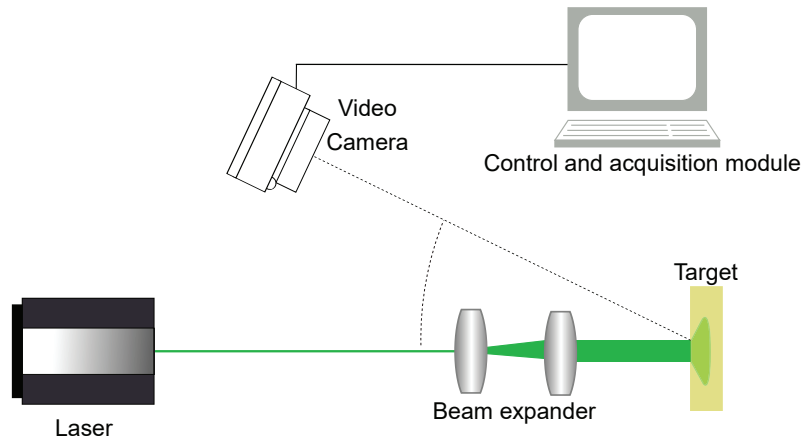
Fig. 1. Typical LSI instrumentation set-up.

Fig. 2. Synthetic laser speckle pattern of a static target.

When the imaged target is moving or contains dynamic scatters, the resultant speckle pattern changes. These type of patterns are called dynamic speckle patterns and they are the ones that we are interested in when assessing macrocirculatory parameters. In practical applications, the video camera used to image the pattern has a finite exposure time. During this time, the camera integrates all the different reflected speckle patterns. The integration of these patterns results in a blurred final image. The blurring degree contains information of how much the speckle pattern changed during the integration time.

2.2 Mathematical Description

A simple way to quantify the blurring degree of a speckle image is by computing its contrast. Speckle contrast (K) is usually defined as the quotient between the image standard deviation and the mean intensity [20]:

$$K = \frac{\sigma_s}{\langle I \rangle} = \frac{\sqrt{\langle (I - \langle I \rangle)^2 \rangle}}{\langle I \rangle} \, , \tag{1}$$

where σ_s corresponds to the standard deviation and $\langle I \rangle$ corresponds to the pattern mean intensity. It has been demonstrated that, giving the speckle statistical properties under real conditions, the value of speckle contrast is bounded by the interval [21]:

$$0 \leq K \leq 1 \, . \tag{2}$$

A contrast value of 1 implies a fully developed speckle pattern, which means that the speckles in the pattern are temporally correlated. On contrary, a contrast value of 0 corresponds to a blurred speckle pattern where the speckles changed during the integration time, *i.e.* are temporally decorrelated.

In practical applications, the contrast value of a speckle pattern never reaches the unitary value. The lack of perfect polarization, system imperfections, stability of light source and the speckle averaging on the image detector results in the decrease of the maximum speckle contrast that can be measured [22].

Apart from speckle contrast, a different metric can be used to quantify the speckle pattern changes between consecutive frames. This metric is the two dimensional correlation coefficient and can be defined as:

$$r = \frac{\sum_x \sum_y (A_{xy} - \bar{A})(B_{xy} - \bar{B})}{\sqrt{(\sum_x \sum_y (A_{xy} - \bar{A})^2)(\sum_x \sum_y (B_{xy} - \bar{B})^2)}} \, , \tag{3}$$

where A and B are two consecutive images, $\bar{A}$ and $\bar{B}$ is the average pixel intensity of each image and the indexes x and y the pixel position in the image.

2.3 Experimental Considerations

When developing laser speckle imaging devices and experiments, an important consideration on the speckle size must be taken into account. In order to prevent spatial aliasing, the speckle size should be, at least, two times the pixels size (2 speckles/pixel) in both x and y directions. A following theoretical equation can be used to compute the speckle size of the system [23]:

$$d_{min} \approx 1.2(1 + M)\lambda f/\# \, , \tag{4}$$

where d_{min} corresponds to the minimum speckle diameter, λ is the light wavelengths, M is the imaging system magnification, and $f/\#$ is the imaging lens f-number. Considering this equation, the speckle size can be controlled by changing the imaging system aperture. An empirical way to determine the speckle size is to compute the 2D power spectral density (PSD) of a static speckle pattern and apply the following equation [24]:

$$d_{min} = 2\frac{l_{PSD}}{d_{energy}} \, , \tag{5}$$

where l_{PSD} is the power spectral density width, in pixels and d_{energy} is the diameter of the energy band.

32

3 Macrocirculation Physiology

Regarding the macrocirculation, some of the most important physiological parameters can be highly summarized as the blood pressures (systolic and diastolic), the pulse wave velocity, and the profile of the pulse waveform. In this work we have been focused on extracting the pulse pressure waveform because it is the parameter that can be measured using laser speckle optical methods.

The pulse pressure waveform is not constant along all the arterial tree. Both its shape and intensity changes, starting with a strong pulsation component at the major arteries and ending in a static pressure value at the capillaries. The valuable information on the pulse waveform is encoded in its shape so it is mandatory to assess major arteries. The aorta should be the right choice because it is closer to the heart and produces higher SNR but, in order to assess it, an invasive probe will be necessary. Since we are interest in non-invasive instrumentation, arteries like the carotid or radial must be used because they are superficial and still contain valuable information.

The aortic pulse pressure profile is detailed in figure 3. The systolic peak corresponds to the highest pressure value, the dicrotic notch is induced by the aortic valve closure and, the diastolic pressure corresponds to the minimum pressure value [25]. This figure corresponds to a typical profile from an unhealthy subject because the reflected wave, also represented in the figure, appears before the systolic peak, resulting in an increase of the maximum pressure [26].

By identifying these feature points (systolic peak, reflected wave, dicrotic notch) many important parameters can be extracted even when the pressure waveform is not amplitude calibrated. This method, called pulse waveform analysis (PWA), can determine many indices of the cardiovascular function like the Augmentation index (AIx), Ejection Time Index (ETI), Subendocardial Viability Ratio (SEVR %), maximum rate of pressure change (dP/dt_{max}) and area under the curve (AUC) [26].

Apart from these parameters that can be extracted by PWA, the pulse waveform velocity (PWV) can only be computed by assessing two pulse pressure waveform in different sites. This parameters corresponds to the propagation velocity of the pulse waveform and can be determined by computing the time delay between the detection of the same pulse waveform in two sensors separated by a known distance.

In this work, the computations of these parameters were not performed since our aim it to focus on instrumentation development and proof of concept. However, it is important to understand why this field has clinical relevance and what type of information can be extracted from this data.

4 Experimental Methods

Three different tests have been developed during this work in order to test the ability of LSI to extract the pulse pressure waveform. In the first test, three different light wavelengths have been tested in order to select the better one [28]. In the second experiment, only the best wavelength was used and the group of volunteers has been extended [29]. The last experiment consists in a pilot study that used LSI in order to segment a target with longitudinal motion [30]
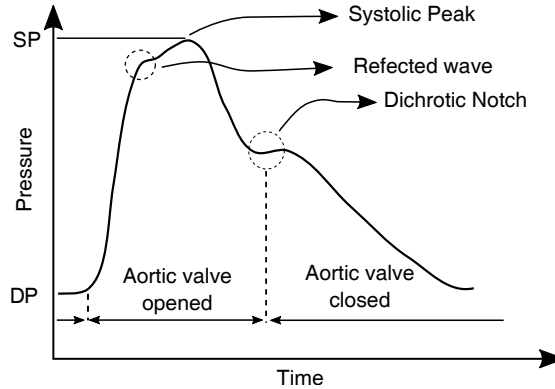
Fig. 3. Aortic pressure waveform. SP - Systolic pressure. DP - Diastolic pressure [27].

4.1 Multiwavelengths Study

The experimental set-up described in subsection 2.1 was used to study which wavelength is better to extract the pulse waveform. The target on this set-up was replaced by a phantom that tries to mimic the radial artery motion, which is the primary site for the application of this method. The phantom was built by stacking 4 white translucent silicone membranes with a total thickness of 2 mm and a size of 30 mm $\times$ 60 mm (W $\times$ H). It has been attached to a controlled piezoelectric actuator that reproduced sinusoidal movements with different amplitudes and frequencies. The phantom is depicted in figure 4.

The phantom was actuated with amplitudes ranging from 2 peak-to-peak voltages (V_{pp}) to 8 V_{pp} and frequencies ranging from 1/5 Hz to 1 Hz. These combinations of parameters lead to phantom maximum displacements of 0.75 mm and velocities up to 2.35 mm/s.

Three different light sources have been used in this experiment: a green laser diode (L_{532}), Thorlabs ref. CPS532, with a wavelengths of 532 nm, with optical power of 4.5 mW and with an output circular beam; a red laser diode (L_{635}), Coherent inc. ref. VHK, with a wavelength of 635 nm, with an optical power of 4.9 mW and, with a circular beam; and a near infra-red laser diode (L_{850}), with a wavelength of 850 nm, with an optical power of 3mW, and with a focusable elliptical beam.

Finally, a monochrome video camera (Pixelink - B741U), attached to a fixed focal lengths lens (50 mm), was used to image the speckle patterns. By using equation (4), the optimal f-number to ensure a correct sampling (4 pixels/speckle) was computed and corresponds to f/16. The camera has been set-up to a resolution of 1280 $\times$ 1024 pixels, with an exposure time of 15 ms and with a frame rate of 15 frames per second (fps). The acquisition time has been 7 seconds for all the acquisitions.

The speckle patterns have been processed using the two dimensional correlation coefficient detailed in equation (3). This processing technique only requires the computation of one coefficient for each image pair. In order to easy visualize the data, the correlation coefficient was normalized between 0 and 1 (r') and inverter ($1 - r'$).
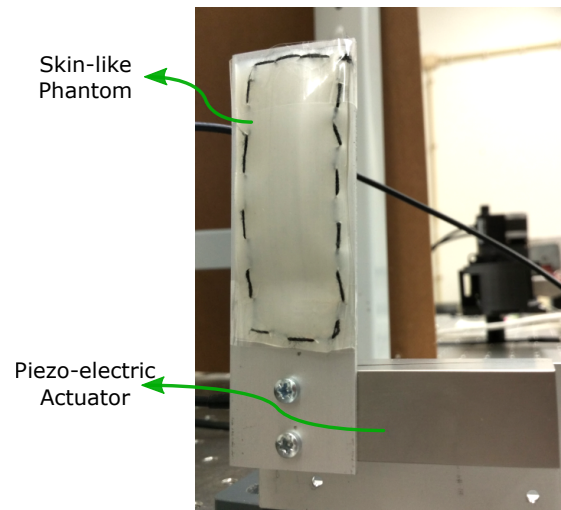
Fig. 4. Photography of the skin-like phantom connected to the piezo-electric actuator [27].

After the bench experiment, a small *in vivo* study was also performed by assessment the radial artery of two healthy volunteers. The volunteers have provided written informed consent prior to participation. Due to the complexity of the biological systems, the video cameras frame rate was increased to 50 fps and the image resolution decreased to 320×240 pixels due to the hardware limitation. For each subject, 9 acquisitions have been performed, three for each laser source, after a 5 minute rest. Each acquisition last for 10 seconds. A photopletismography (PPG) probe was used to assess the pulse waveform but due to synchronization problems both signals could not be visualized at the same time.

4.2 *In vivo* Study

The *in vivo* study has been developed in order to test the better laser light source in a more intensity experiment and using the same processing methods used for LSI microcirculation assessment. Figure 5 shows the experimental setup including the video camera, the beam expander, the subject arm and the PPG probe. In this study, the PPG signal ($PPG(t)$) has been synchronized with the LSI signal which has allowed a better comparison between both. This test was performed in 10 subjects with 3 acquisitions per subject. Each acquisition lasts 10 seconds.

Unlike the previous experiment, in this study, the LSI data was processed using the speckle contrast method (equation (1)). One contrast value for each LSI image has been computed. Again, the contrast values (K(t)) have been inverted (K'(t)) due to the inverse relation between speckle contrast and motion, and normalized between -1 and 1. The signal obtained with the PPG was also normalized in order to facilitate the comparison.

For each acquisition, the heart rate (HR) of the subject was computed by using the fast Fourier transform (FFT) algorithm and identifying the predominant frequency. The data similarity has been assessed by computing the spectral coherence between both signals by using the magnitude-squared coherence function:
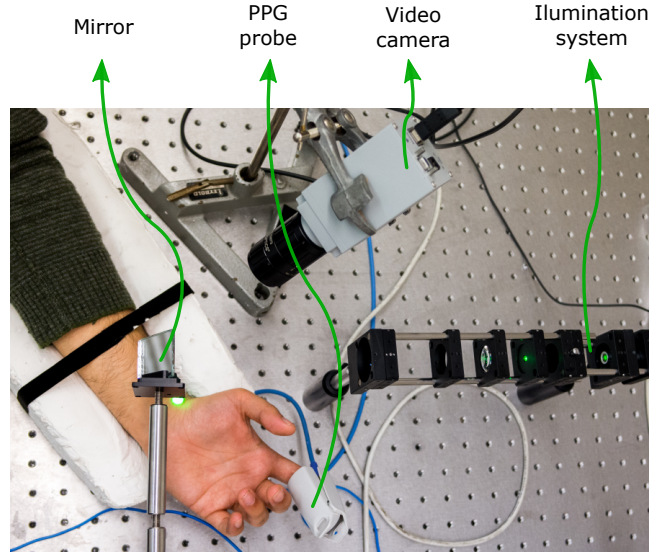
Fig. 5. *In vivo* acquisition scheme for laser speckle imaging and PPG recording.

$$C_{KP}(f) = \frac{|P_{KP}(f)|^2}{P_K(f)P_P(f)} \ , \tag{6}$$

where $P_{KP}(f)$ is the cross-spectral power between $K(t)$ and $PPG(t)$, while $P_K(f)$ and $P_P(f)$ are the PSD of $K(t)$ and $PPG(t)$, respectively. A similarity index (SI) (equation (7)) was then defined as the integral of the magnitude-squared coherence function between 0 and 10 Hz because this band contains the relevant information:

$$SI = \int_0^{10} C_{KP}(f)df \ . \tag{7}$$

4.3 Image Segmentation Study

The last study has been developed in order to explore the possibility of LSI to identify and segment targets with longitudinal motion without any stereoscopic data or other types of sensors. This type of movement is difficult to identify because it occurs on the imaging axis but speckle methods can be useful in these situations. Moreover, this pilot study aims at segment a target with specular reflection similar to skin and soft tissues.

For this test, the apparatus described in figure 1 was modified in order to include a second target. The new target, identical to the first one, has been placed next to the original one. A small gap of 3 mm was left between the targets. The main idea behind this new phantom was to have two identical independent membranes, one connected to the piezoelectric actuator and other completely static. The moving membrane was actuated with a sinusoidal movement with frequencies of 1, 1/2, 1/3 and 1/5 Hz and amplitudes of 1, 2, 4 and 6 V_{pp}.

36

In this test, the used light source was the L_{635} with a video camera resolution of 1280×1024 pixels and an exposure time of 15 ms. The speckle patterns have been processed using a temporal backward difference in order to enhance the changes between consecutive patterns. The result was then normalized between 0 and 255 and can be defined as:

$$\Delta I(x, y, t) = \frac{I(x, y, t) - I(x, y, t - 1) + 255}{2} \, ,$$ (8)

where $\Delta I(x, y, t)$ is the derivative of the pixel with the position (x, y) and time t.

After this step, the segmentation was performed by computing the regional entropy (RE) of the difference image (ΔI). The regional entropy is an algorithm that computes the entropy of small regions within the complete image with full overlap. In this algorithm, this small regions have been tested for 4 different sizes, 3×3, 9×9, 27×27, and 81×81. For each region, the RE can be computed as:

$$RE = - \sum_{bin=0}^{255} P_{bin} \times log_2(P_{bin}) \, ,$$ (9)

where P_{bin} is the probability of the occurrence of a pixel with value bin in the region. The bin values range from 0 to 255.

The produced two dimensional entropy map is finally segmented by applying a threshold. Pixels with entropy above this value have been classified as moving (1) and pixels with entropy below this value have been classified as non-moving (0). The flow-chart of this algorithm is presented in figure 6.

The most suitable region size has been determined by computing the sensitivity (SE) and specificity (SP) for thresholds between 0 and 6 (the maximum value of entropy computed in this experiment) with steps of 0.05. With these data, a receiver operatic characteristic (ROC) curve has been plotted and its area under the curve (AUC) determined. The region with higher values of AUC has been considered as the most suitable one.

A data-set of 12 entropy maps, containing membrane velocities from 0 to 1763 $\mu m s^{-1}$, was used to determine which threshold will lead to better results. This data-set was selected in order to fully cover the range of membrane velocities presented in this experiment. The best threshold corresponds to the one that maximizes the mean accuracy (AC) of this training data-set.

Finally, the best region size and threshold have been applied to a test data-set composed of 5 videos with different parameters (1 Hz-$1V_{pp}$, 1 Hz-$4V_{pp}$, 1/2 Hz-$6V_{pp}$, 1/3 Hz-$4V_{pp}$, and 1/5 Hz-$1V_{pp}$). For each video, the AC, positive and negative predictive ratios (PPV and NPV), and Matthews correlation coefficient (MCC) have been computed [30].

5   Experimental Results

This section presents the results of the experiments described in section 4.

Start

Get speckle data

1280 x 1024
15 fps
Skin-like phantom

Temporal
Derivative

Regional
entropy

Optimal region size
determined using
ROC curve

Binarization
based on threshold

Optimal threshold
determined using
traning data-set

Manually segmented
mask

Determination of
performance
parameters

End
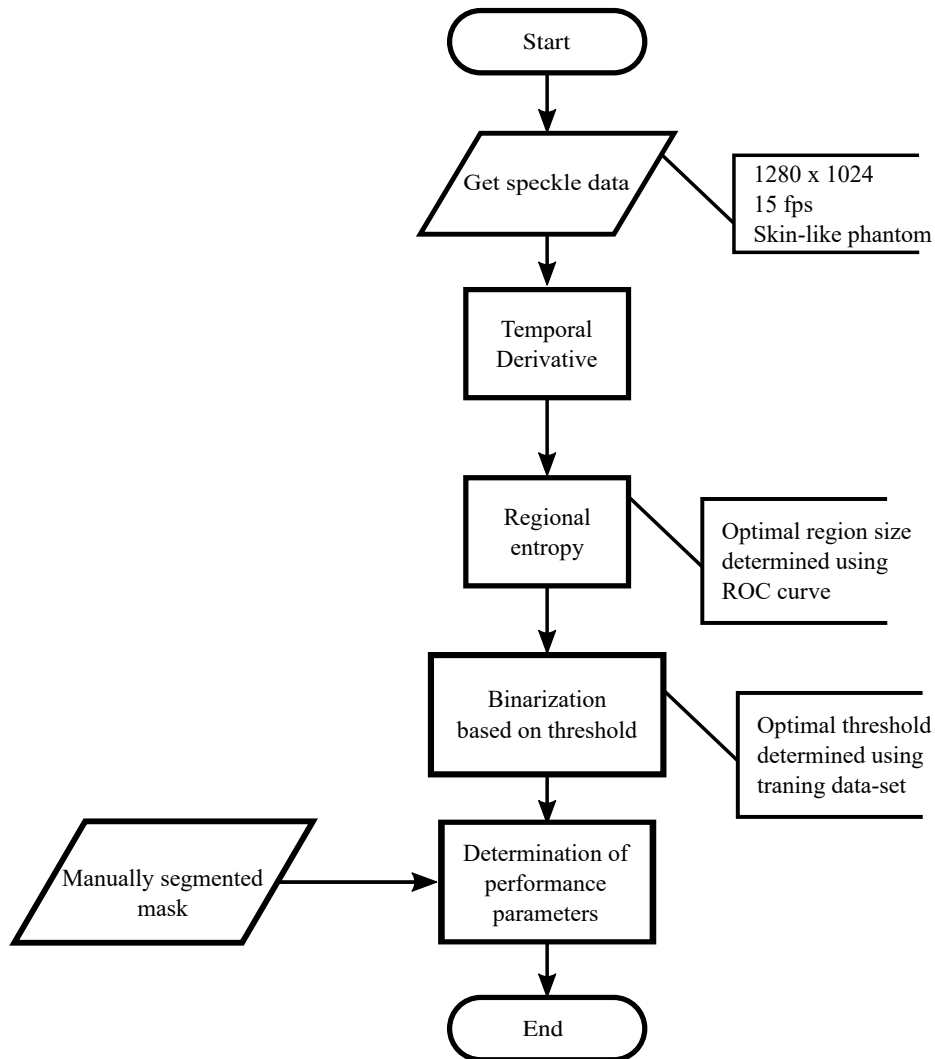
Fig. 6. Flowchart of the method used to segment the moving skin-like phantoms.

5.1 Multiwavelengths Study

The raw speckle data have been processed and compared with the electrical signal applied to the phantom. The figure 7 represents an example of a reconstruction of the velocity profile based on the computation of the speckle correlation coefficient. The blue line corresponds to the velocity profile computed from the piezoelectric stimulation signal. The red line corresponds to the inverse of the correlation coefficient normalized between 0 and 1. Both profiles are very similar which demonstrates the ability of LSI to extract the vibration profile of a skin-like phantom.
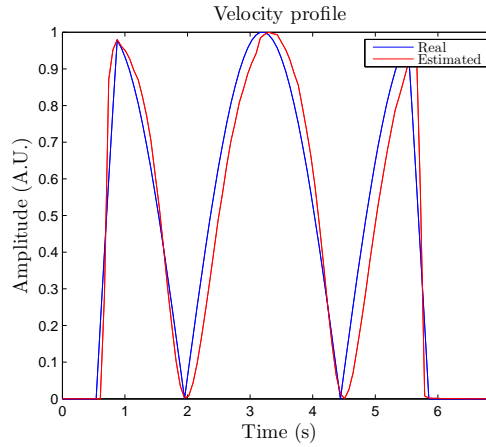
Fig. 7. Plot of $1 - r'$ along time (red line) and absolute velocity of the phantom (blue line) of the movement with amplitude of $2\,V_{pp}$ and 5 seconds of period.

The numerical result for all the movement parameters and lasers sources are presented in table 1. This values corresponds to the root mean square error (RMS) between the real profile and the extracted profile. By analyzing the results for L_{532} we can see that larger periods are reconstructed with lower errors. This can be explained because lower periods corresponds to higher membrane velocities and, due to the hardware limitations on the frame rate (15 fps), faster movements are not acquired in good conditions. For the case of L_{635} light source, the errors decrease for movements with large periods and small displacements. The explanation for this effect is the same as before. Finally, the L_{850} light source does not follow the other two cases because movements with higher amplitudes present lower errors.

The overall errors for the three cases are close to each other with mean errors of 13.8%, 19.6% and 15.8% for L_{532}, L_{635} and L_{850} respectively. However, it can be concluded that the three laser sources have been able to reproduce the membrane velocity profile with good results. Having said that, all the sources have been used in the *in vivo* experiment.

The *in vivo* test lead to a different conclusion. First, all the laser sources presented much lower SNR compared with the bench experiments. Moreover, the L_{850} was unable to record the pulse waveform of the two subjects. This occurred due to differences in the optical properties of the skin-like phantom and the real tissue. In the human tissue, the penetration and dispersion of the infra-red light is higher than in the phantom.

Figure 8 presents an example of two pulse waveforms extracted from L_{532} (a) and L_{635} (b). The periodic nature of the pulse waveform is clearly identified in both figures. The predominant oscillation frequency corresponds to the subject heart rate. In figure 8-(a) some pulse waveform features, like the systolic peak and dicrotic notch can also be identified.

The numerical results of the HR determination are presented in table 2. The acquisition number S3 has been corrupted with motion artifacts which explains the large error between the subject HR and speckle HR. The variable $g\,\epsilon_{rms}$ represents the global error of each light source computed by the root mean square (rms) method. If the acquisition

Table 1. Results of the RMS error of the velocity profile reconstruction with L_{532}, L_{635} and L_{850} data. Values are presented in percentage.

	Period (s)	Amplitude (V_{pp})		
		2	4	8
L_{532}	1	20.68	11.87	19.31
	2	18.63	15.08	12.68
	3	15.55	9.92	9.52
	5	12.22	9.45	10.21
L_{635}	1	17.38	18.96	19.58
	2	20.83	21.68	24.91
	3	12.54	20.66	25.11
	5	10.31	16.78	26.64
L_{850}	1	16.27	14.78	13.26
	2	16.11	12.19	13.83
	3	20.42	13.97	9.02
	5	21.62	22.64	14.89

Table 2. Results of heart rate (HR) estimation with *in vivo* conditions. The values in the table are expressed in beats per minute (bpm). * Data-set tainted by artifacts.

	Data set	S1	S2	S3*	S4	S5	S6	$g\ \epsilon_{rms}$
L_{532}	Subject HR	62.3	62.3	64.1	65.9	67.8	67.8	
	Speckle HR	61.4	62.4	69.6	65.7	67.6	67.2	0.50 (2.28)
	Data set	S7	S8	S9	S10	S11	S12	$g\ \epsilon_{rms}$
L_{635}	Effective HR	64.1	65.9	67.7	82.4	89.7	60.4	
	Speckle HR	66.4	66.0	68.7	82.4	88.6	59.6	1.15

S3 is excluded from the analysis, the $g\ \epsilon_{rms}$ for the L_{532} is much lower then the global error of the L_{635}, 0.5 bpm compared with 1.15 bpm.

These results in addition to the better graphical representation of figure 8 leads to the conclusion that L_{532} is the one that can extract the pulse waveform with higher SNR. The lower tissue penetration of L_{532} can explain why this was the wavelengths with better results. For that reason, this light source was used in the second, more intensity, *in vivo* study.

5.2 *In vivo* Study

In the second study, the speckle contrast was used as processing method in order to match the signal processing technique already used by LSI commercial devices. Figure 9 presents an example of two speckle images captured at different cardiac cycle stages. The speckle pattern of the stage when the artery is moving appears more blurred than the speckle pattern when the artery is stopped, resulting in a contrast decrease of figure 9(a).

An example of the contrast values and the PPG data is shown on figure 10. The profile of both signals is very similar and the identification of the feature points can be done in the speckle contrast signal. This indicates good compatibility between the two methods. The morphological differences between these signals are expected because

40
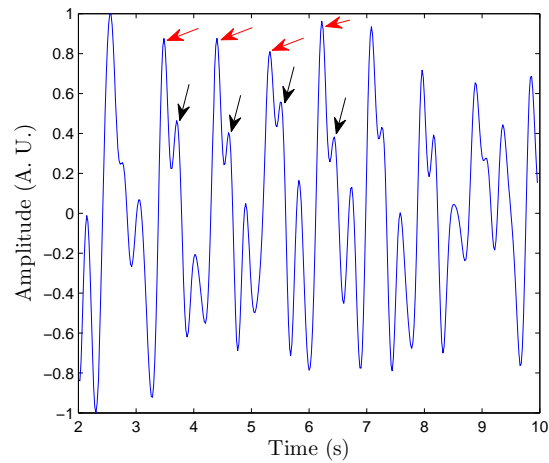
(a) L_{532}
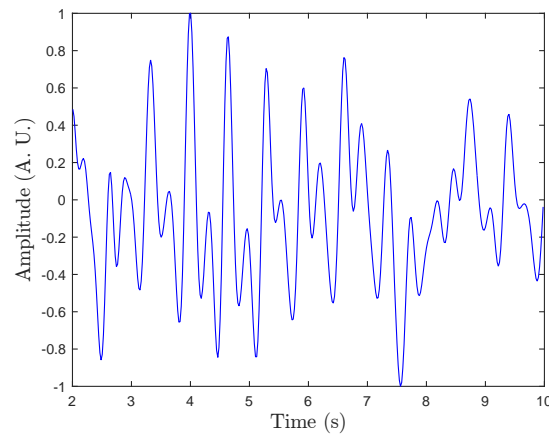
(b) L_{635}

Fig. 8. Output signal of the correlation algorithm to the *in vivo* test S4 (a) and S10 (b). Red arrows show the probable systolic peak and black arrows show the probable dicrotic notch.

they have been acquired in different sites (radial artery *vs* finger tip) which corresponds to different locations on the arterial tree.

The HR identified by the PPG signal was considered as the correct one because photopletismography is a well established technique. The heart rates detected in this study range from 55 to 84 bpm with a mean value of 67 bpm corresponding to a normal rest condition. The HR values for both speckle and PPG signal have been plotted in figure 11(a). The linear fitting is almost collinear with the 45 degree line, which demonstrates the very good agreement between both methods. Finally, the root mean square error between PPG HR and speckle HR, for all data-sets, was 1.3 bpm.

The results from similarity index are presented in figure 11(b). It is important to emphasize that PPG and speckle data come from two different sites and two different information sources. However, they both express the effect of blood flowing through

(a) Systole   (b) Diastole
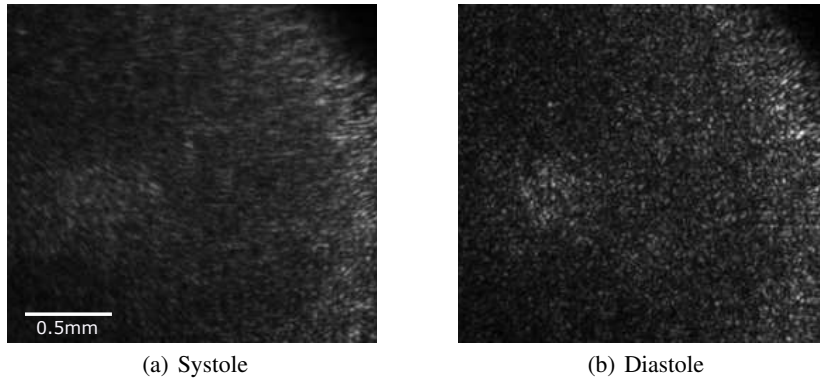
Fig. 9. Laser speckle images from the radial artery at different stages of the cardiac cycle: a) systole, higher skin velocities leading to a blurred speckle image; b) diastole, lower velocities result in a sharper speckle image.
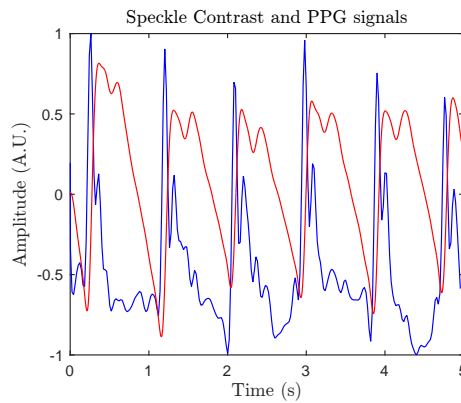
Fig. 10. Temporal representation of PPG data (red line) and speckle contrast data (blue line).

the arterial system. For that reason, it is expected to see spectral similarities between both signals within the range of interest (0-10 Hz). The subject number 1 presents a very good spectral similarity with all its SI above 0.73. On the contrary, subject number 3 and 7 present a SI below 0.5. These values show that the precision of the pulse waveform extraction depends on the analyzed subject. This can be possibly explained due to the physiological differences between each volunteer, like the blood pressure and fatty layer. Subjects with lower pressure or large fatty layer lead to a less pulsatile artery, resulting in lower speckle SNR.

5.3   2D Image Segmentation

The last experiment of this work corresponds to the ones of the 2D image segmentation study. First, the 4 processing window sizes have been applied to all the data in order to determine which size performs better. The results have been plotted in figure 12(a). From this graphic we can conclude that all the methods show very good results with

42

(a)   (b)
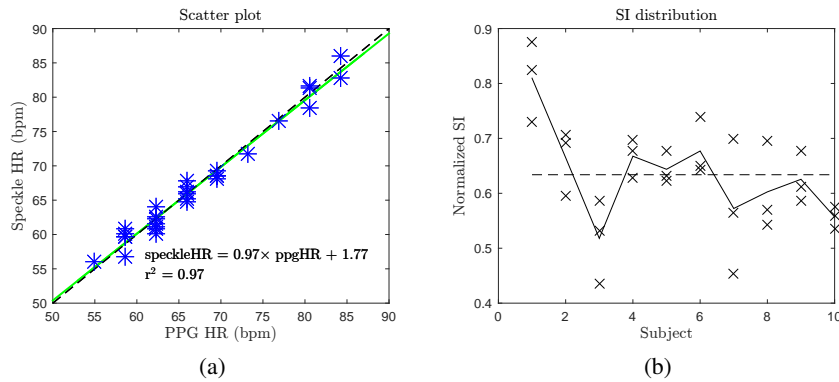
Fig. 11. Data analysis: a) HR scatter plot of the PPG HR vs speckle HR. Each star represents one data set. The black line correspond to the fitting equation and the green line to the first quadrant bisector. b) Scatter plot of the similarity index (SI) for each subject. The dashed line represents the total mean and the solid line the subjects mean.

AUC of 0.97, 0.99, 0.99 and 0.98 for window sizes of $3{\times}3$, $9{\times}9$, $27{\times}27$, and $81{\times}81$ respectively. However, the intermediate sizes have achieved a performance slightly better and, since the smaller window sizes are fast to compute, the method with the window size of $9{\times}9$ can be considered the better one.

After the selection of the best method, the training data-set has been used to select the best threshold. In oder to achieve this, all the possible thresholds (0-6) were applied to all the data-set images. The results for each threshold and image was compared with a manually segmented mask in oder to compute the accuracy of the method. This data is represented in figure 12(b) where each line represents the evolution of the accuracy for each data-set image. The best threshold has been determined by computing the maximum mean accuracy for all the data-set (bold line of figure 12(b)) and corresponds to 2.95.

Figure 13 shows two segmented images of the moving membrane, one manually (figure 13(a)) and the other using the automatic entropy based method (figure 13(b)). The equivalence between both segmentations is evident and, in fact, the entropy based method could segment even a larger area of the membrane. The black vertical line corresponds to a dark zone where speckle pattern is not visible (please consult [30] for more details).

The results of the applications of this method to the validation data-set are presented in table 3. From this results, it can be concluded that all the evaluation metrics achieved very good values. In this type of data, there are much more stopped pixels than moving pixels (class unbalancing) and, in these cases, the MCC must be used to assess the method quality. This metric ranges from -1 to 1, meaning complete agreement (1), complete disagreement (-1), and random classifier (0). In this validation data-set, the MCC range from 0.84 to 0.95 which indicates a very good classifier. Regarding the accuracy, it can be highlighted that at leas 95% of all the image pixels have been correctly classified.

(a) (b)
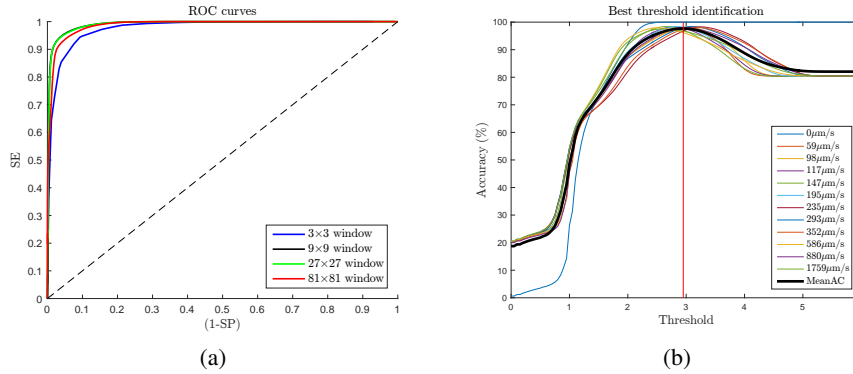
Fig. 12. Model optimization: (a) Best element size identification using ROC curves. SE stands for sensibility and SP for specificity. (b) Best threshold identification for the 9×9 method using 12 images of the training data-set. The vertical red line represents the best threshold (2.95).

Fig. 13. Output of the application a 2.95 threshold.

Table 3. Results in the validation data set-for a window of 9×9 pixels.

Movement	Max. Vel. (mm/s)	AC (%)	PPV(%)	NPV(%)	MCC	No. frames
1/5 Hz - $1V_{pp}$	0.06	96.54	86.26	99.03	0.8872	30
1 Hz - $1V_{pp}$	0.29	98.73	96.16	99.21	0.9519	15
1/3 Hz - $4V_{pp}$	0.59	97.57	94.95	98.13	0.9178	45
1/2 Hz - $6V_{pp}$	0.88	95.80	92.96	96.33	0.8512	30
1 Hz - $4V_{pp}$	1.17	95.14	78.04	99.34	0.8416	15

6 Conclusion

This chapter presented three different studies that demonstrate the capacity of LSI to assess macrocirculatory information. These experiments were initiated by using a bench phantom that mimics the arterial vibrations and ended in real *in vivo* applications using the same methods used in commercially available LSI devices.

All the results demonstrated that LSI can be used with good reliability to extract macrocirculation parameters. The main purposes of this project was to proof that the available LSI devices that are used for microcirculation assessment could also be used for macrocirculation assessment without making big hardware and software changes.

44

With the inclusion of this feature in LSI devices, a new macro-micro circulatory joint information could be assessed and explored.

References

1. Ozcan, A., Bilenca, A., Desjardins, A.E., Bouma, B.E., Tearney, G.J.: Speckle reduction in optical coherence tomography images using digital filtering. Journal of the Optical Society of America. A, Optics, image science, and vision 24 (2007) 1901–1910
2. Grédiac, M.: The use of full-field measurement methods in composite material characterization: interest and limitations. Composites Part A: Applied Science and Manufacturing 35 (2004) 751–761
3. Bendjus, B., Cikalova, U., Schreiber, J.: Material characterization by laser speckle photometry. In: V International Conference on Speckle Metrology. Volume 8413., Vigo, Spain, SPIE (2012) 841315
4. Fercher, A., Briers, J.: Flow visualization by means of single-exposure speckle photography. Optics Communications 37 (1981) 326–330
5. Boas, D.a., Dunn, A.K.: Laser speckle contrast imaging in biomedical optics. Journal of biomedical optics 15 (2010) 011109
6. Parthasarathy, A.B., Tom, W.J., Gopal, A., Zhang, X., Dunn, A.K.: Robust flow measurement with multi-exposure speckle imaging. Optics express 16 (2008) 1975–89
7. Kazmi, S.M.S., Wu, R.K., Dunn, A.K.: Evaluating multi-exposure speckle imaging estimates of absolute autocorrelation times. Optics letters 40 (2015) 3643–3646
8. Ramirez-San-Juan, J., Regan, C., Coyotl-Ocelotl, B., Choi, B.: Spatial versus temporal laser speckle contrast analyses in the presence of static optical scatterers. Journal of Biomedical Optics 19 (2014) 106009–106009
9. Zakharov, P., Völker, A.C., Wyss, M.T., Haiss, F., Calcinaghi, N., Zunzunegui, C., Buck, A., Scheffold, F., Weber, B.: Dynamic laser speckle imaging of cerebral blood flow. Optics express 17 (2009) 13904–13917
10. Varma, H.M., Valdes, C.P., Kristoffersen, A.K., Culver, J.P., Durduran, T.: Speckle contrast optical tomography: A new method for deep tissue three-dimensional tomography of blood flow. Biomedical Optics Express 5 (2014) 1275–1289
11. Huang, C., Irwin, D., Lin, Y., Shang, Y., He, L., Kong, W., Luo, J., Yu, G., Huang, C., Irwin, D., Lin, Y., Shang, Y., He, L., Kong, W.: Speckle contrast diffuse correlation tomography of complex turbid medium flow. Medical physics 42 (2015) 4000–4006
12. Senarathna, J., Member, S., Rege, A., Li, N., Thakor, N.V.: Laser Speckle Contrast Imaging : Theory , Instrumentation and Applications. Biomedical Engineering, IEEE Reviews in 6 (2013) 99–110
13. Briers, D., Duncan, D., Kirkpatrick, S., Larsson, M., Stromberg, T., Thompson, O.: Laser speckle contrast imaging : theoretical and practical limitations. Journal of Bomedical Optics 18 (2013) 1–9
14. Vaz, P.G., Humeau-Heurtier, A., Figueiras, E., Correia, C., Cardoso, J.: Laser speckle imaging to monitor microvascular blood flow: a Review. IEEE Reviews in Biomedical Engineering In press (2016) 1–1
15. Liu, J., Zhang, H., Lu, J., Ni, X., Shen, Z.: Quantitative model of diffuse speckle contrast analysis for flow measurement. Journal of Biomedical Optics 22 (2017) 76016
16. Ponticorvo, A., Burmeister, D.M., Rowland, R., Baldado, M., Kennedy, G.T., Saager, R., Bernal, N., Choi, B., Durkin, A.J.: Quantitative long-term measurements of burns in a rat model using Spatial Frequency Domain Imaging (SFDI) and Laser Speckle Imaging (LSI). Lasers in Surgery and Medicine 49 (2017) 293–304

17. Liu, Q., Chen, S., Soetikno, B., Liu, W., Tong, S., Zhang, H.: Monitoring acute stroke in mouse model using laser speckle imaging-guided visible-light optical coherence tomography (2017)
18. Zakharov, P.: Ergodic and non-ergodic regimes in temporal laser speckle imaging. Optics Letters 42 (2017) 2299–2301
19. Kirkpatrick, S., Duncan, D., Wang, R., Hinds, M.: Quantitative temporal speckle contrast imaging for tissue mechanics. Journal of the Optical Society of America. A, Optics, image science, and vision 24 (2007) 3728–3734
20. Duncan, D.D., Kirkpatrick, S.J.: Can laser speckle flowmetry be made a quantitative tool? Journal of the Optical Society of America. A, Optics, image science, and vision 25 (2008) 2088–2094
21. Briers, J.D., Fercher, A.F.: Retinal blood-flow visualization by means of laser speckle photography. Investigative ophthalmology & visual science 22 (1982) 255–259
22. Thompson, O., Andrews, M., Hirst, E.: Correction for spatial averaging in laser speckle contrast analysis. Biomedical Optics Express 2 (2011) 1021–1029
23. Ennos, A.E.: Speckle interferometry. In: Laser Speckle and Related Phenomena. Volume 9 of Topics in Applied Physics. Springer Berlin Heidelberg (1975) 203–253
24. Khaksari, K., Kirkpatrick, S.J.: Combined effects of scattering and absorption on laser speckle contrast imaging. Journal of Biomedical Optics 21 (2016) 76002
25. Williams, B., Lacy, P.S., Thom, S.M., Cruickshank, K., Stanton, A., Collier, D., Hughes, A.D., Thurston, H., O'Rourke, M.: Differential impact of blood pressure-lowering drugs on central aortic pressure and clinical outcomes: Principal results of the Conduit Artery Function Evaluation (CAFE) study. Circulation 113 (2006) 1213–1225
26. Pereira, T., Santos, I., Oliveira, T., Vaz, P., Correia, T., Pereira, T., Santos, H., Pereira, H., Almeida, V., Cardoso, J.: Characterization of optical system for hemodynamic multi-parameter assessment. Cardiovascular Engineering and Technology 4 (2013) 87–97
27. Vaz, P.: Methods for hemodynamic parameters measurement using the laser speckle effect in macro and microcirculation. Phd thesis (available online with credentials), Universidade de Coimbra (2016)
28. Vaz, P., Pereira, T., Figueiras, E., Correia, C., Humeau-Heurtier, A., Cardoso, J.: Which wavelength is the best for arterial pulse waveform extraction using laser speckle imaging? Biomedical Signal Processing and Control 25 (2016) 188–195
29. Vaz, P., Santos, P., Figueiras, E., Correia, C., Humeau-Heurtier, A., Cardoso, J.: Laser speckle contrast analysis for pulse waveform extraction. In: Novel Biophotonics Techniques and Applications III. Volume 9540., Munich, SPIE (2015) 954006–954007
30. Vaz, P., Pereira, T., Capela, D., Requicha, L., Correia, C., Humeau-Heuertier, A., Cardoso, J.: Use of laser speckle and entropy computation to segment images of diffuse objects with longitudinal motion. In: II International Conference on Applied Optics and Photonics, Aveiro (2014)